PHYSICAL REVIEW A **102**, 033529 (2020)

Selective-frequency-gap-induced negative anisotropic scattering in designer photonic structures with short-range order

Sudhir Kumar Saini and Rajesh V. Nair[*]

Laboratory for Nano-scale Optics and Meta-materials (LaNOM), Department of Physics, Indian Institute of Technology Ropar, Punjab 140001, India

(Received 18 April 2020; accepted 3 September 2020; published 30 September 2020)

Optimizing scattering is the most sought-after goal in wave transport through photonic structures, which opens up many physical processes with prospective applications. Here, we uncover the appearance of a tunable frequency gap with negative anisotropic scattering (g) values in the visible wavelength range using photonic structures with short-range order. A scattering model is devised based on the structural morphology of samples to explain the wavelength-dependent frequency gap and the g values. We show complete agreement between the experiment and theory, which is supported by the structure factor calculations. Specifically, we find a g value of -0.7 ± 0.2 at the frequency gap in accordance with theoretical calculations. The study puts forward an amenable approach for tailoring the scattering anisotropy values using photonic structure with short-range order and thus mediates an inclination toward the localization.

DOI: 10.1103/PhysRevA.102.033529

I. INTRODUCTION

Controlling the wave transport associated with electrons, phonons, and photons at the respective subwavelength scale offers rich unexpected physical processes with unparalleled applications [1,2]. The presence of an electronic band gap in semiconductors provides the control of electron transport with a remarkable breakthrough in the electronic industry [3]. Similarly, the subwavelength optical systems ranging from photonic crystals to metamaterials provide a platform to control the photons for their guiding and manipulation in optical communication and lasers [4]. Long-range periodic ordering of atomic or optical potential is required for the band-gap formation and, therefore, both systems are analogous to each other.

Recently it was discovered that electron scattering due to random perturbations in the atomic potential induces processes such as finite resistivity and Anderson localization [5,6]. Similarly, disordered optical potential induced by the random variation in dielectric constants is proposed for light localization with prospective applications [7–9]. Light transport through a disordered sample is described using the diffusion approximation in terms of scattering (l_s) and transport (l_t) mean free paths with an effective refractive index (n_{eff}) and finite thickness (L) such that $l_t \ll L$ [10]. Further, the scattering can be isotropic or anisotropic depending on the value of scattering anisotropy factor (g) which is defined as the average of the cosine of the scattering angle (θ) and $g \equiv \langle \cos(\theta) \rangle$ which is related to l_t by the relation $l_t = \frac{l_s}{1-g}$. The scattering regime is also classified based on the morphology of the sample. If the separation between the scatterers is larger than the incident wavelength, then an independent scattering approximation is considered with $l_s = \frac{1}{n\sigma}$ where n is the number density of scatterers and σ is the scattering cross section defined as $\sigma = \int \frac{d\sigma}{d\Omega}(1 - \cos\theta)d\Omega$ [11].

The spacing between the scatterers reduces with an increase in the n value and their spatial positions develop a structural correlation, which leads to local interference [12]. The structural correlation was used in an ion-ion repulsion model to estimate the resistivity of liquid metal using the structure factor $S(q)$ [13]. Thus, the modified scattering cross section (σ^*) which includes the $S(q)$ is given by $\sigma^* = \int \frac{d\sigma}{d\Omega}(1 - \cos\theta)S(q)d\Omega$. It has been asserted that the structural correlation can lead to large l_t values with high conductivity for disordered liquid metals and transparency of the cornea [14,15]. Similarly, the spatial correlation among subwavelength scatterers also leads to the phase correlation in the scattered light with $\sigma^* < \sigma$ [16]. However, it was pointed out through theoretical as well as experimental studies that a photonic system with short-range order can exhibit an enhanced σ^* with negative g values [17]. Some studies have also emphasized the control of l_t values in a particular wavelength range using the spatial correlation among scatterers [18–23]. Such a spatially correlated photonic structure with short-range order can exhibit frequency gaps with exceptional scattering properties and has applications in coloration and lasing [24–31].

In this paper, we discuss the tunable frequency gap in a three-dimensional (3D) photonic structure with short-range order having monodisperse submicron scatterers. We devise a scattering model based on the structural morphology of the sample to discuss the frequency gap. The wavelength-dependent scattering lengths are estimated along with structure factor calculations to corroborate the frequency gap. Further, we found a negative anisotropic scattering regime in the range of the frequency gap that is in complete agreement with theory, which is a much sought-after goal in scattering systems.

---

[*] rvnair@iitrpr.ac.in

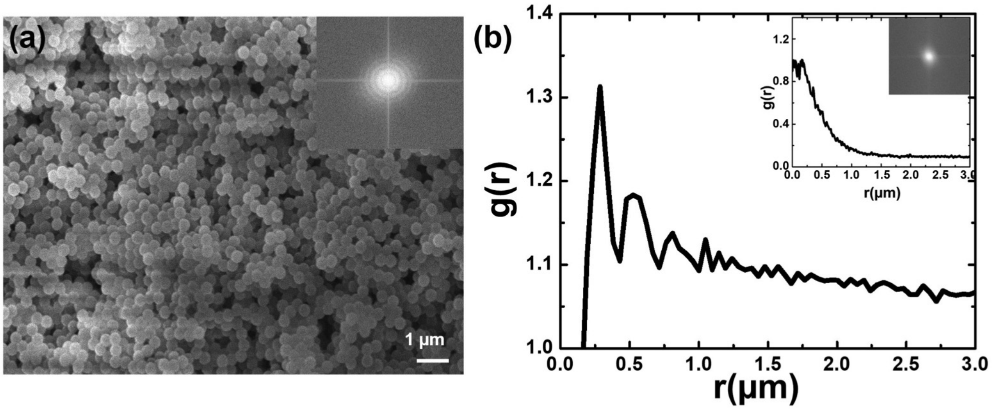

FIG. 1. (a) SEM image of the PS287 sample that shows the clusters consist of monodisperse scatterers. The FT image in the inset shows the ring formation due to the presence of short-range order. (b) The radial distribution function [$g(r)$] shows the periodic oscillations until $r \leqslant 1\,\mu$m which also indicates the presence of short-range order. Inset: The $g(r)$ for the reference sample shows the absence of oscillations due to the lack of any local structural order and the FT image also depicts a bright spot at the center without any ring formation.

II. RESULTS AND DISCUSSION

The 3D photonic sample with short-range order is synthesized using an optimized self-assembling method. The sample consists of monodisperse polystyrene (PS) beads (scatterers) on a glass microslide. A custom-built hollow Teflon cylinder is used to control the sample dimensions. The PS beads are charge stabilized in the suspension. The repulsive Columbic forces between the negatively charged PS beads are compensated by the controlled addition of positive electrolyte so that the flocculation occurs during the self-assembling process. We found 0.1 M of positive electrolyte ($CaCl_2$) is sufficient to induce the flocculation in the PS suspension to form the clusters with short-range order.

The synthesis process can be precisely controlled using the electrolyte concentration. Samples are synthesized using different beads with varying diameters (d) and the concentration of the beads is varied to achieve samples with varying fill fraction (ϕ) for a specific d value (see Appendix A). The value of ϕ signifies the amount of scatterers present in the sample and an optimal value of ϕ is essential to induce the spatial correlation between the scatterers. Figure 1(a) shows the scanning electron microscope (SEM) image of the sample made using PS scatterers with d value of 287 ± 10 nm (PS287). The scatterers are connected to form clusters with local short-range order in the submicron scale as seen in the SEM image. The inset in Figure 1(a) shows the Fourier transform (FT) of the SEM image that shows the concentric rings which validate the short-range order with no long-range translational symmetry [24]. Figure 1(b) shows the radial distribution function [$g(r)$] which is characterized by damped oscillations as a function of spatial interval r. The nearest scatterer-scatterer distance is estimated to be 280 nm in close agreement with the d value of the PS287 sample. The second and third peaks occur at $r \approx 0.5$ and 0.8 µm which correspond to $r \approx 2d$ and $3d$, respectively, which also confirms the short-range periodicity of scatterers. The periodic oscillations decay faster for $r > 1\,\mu$m due to the lack of long-range order. Such oscillations are absent for the TiO_2 sample which consists of polydisperse scatterers as shown in the Fig. 1(b) inset. The ringlike pattern is also absent in the FT image for the TiO_2 sample [Fig. 1(b) inset] due to the lack of any order and hence is taken as a "reference" sample.

When the light impinges on such a sample, it is multiply scattered in random directions. Therefore, to account for all the transmission channels, the measurement of wavelength-dependent total transmission is required. A home-built setup equipped with an integrating sphere is used to measure the total transmission of light passing through the samples (see Appendix A). Figure 2(a) shows the measured total transmission spectra for the reference (solid line) and the PS287 sample (dotted line) with an L value of 30 ± 3 µm and $\phi = 0.55$. The reference sample shows the expected monotonic decrease in the total transmittance value with a decrease in wavelength [23]. The PS287 sample shows an interesting wavelength-dependent variation with a noticeable drop in transmitted light at a particular wavelength (λ_g) of 655 ± 5 nm. The transmission value at 655 nm is reduced to 16% in comparison to the same at the long-wavelength limit of 950 nm. The drop in transmission value is originated due to the interference of light induced by the local short-range order supported by the spatial correlation of scatterers and, therefore, we signify the transmission dip as a frequency gap. Such a frequency gap is absent for the reference sample as it does not have structural correlation due to polydisperse scatterers [23].

The dip in transmission spectra is reminiscent of a frequency gap associated with long-range ordered samples such as photonic crystals [24]. If such a concurrence exists, then the transmission dip at λ_g should be tunable with ϕ and d values. To analyze this concurrence, we devise a scattering model based on the structural morphology of the sample inferred from the SEM image to illustrate the frequency gap. The scatterers are spatially connected to form clusters with short-range order within it and, thus, a cluster model is considered which consists of few scatterers as shown in Fig. 2(b). The light with wave vector $\vec{k}_{\text{in}}$ is incident on the cluster that results in a scattered wave with wave vector $\vec{k}_{\text{sc}}$ at an angle (θ). The difference between the two wave vectors corresponds to a spatial momentum vector $\vec{q}$. Since the scattering is elastic, we have $|\vec{k}_{\text{in}}| = |\vec{k}_{\text{sc}}| = k$ that results in $|\vec{q}| = 2k\sin(\theta/2)$ where $k =$

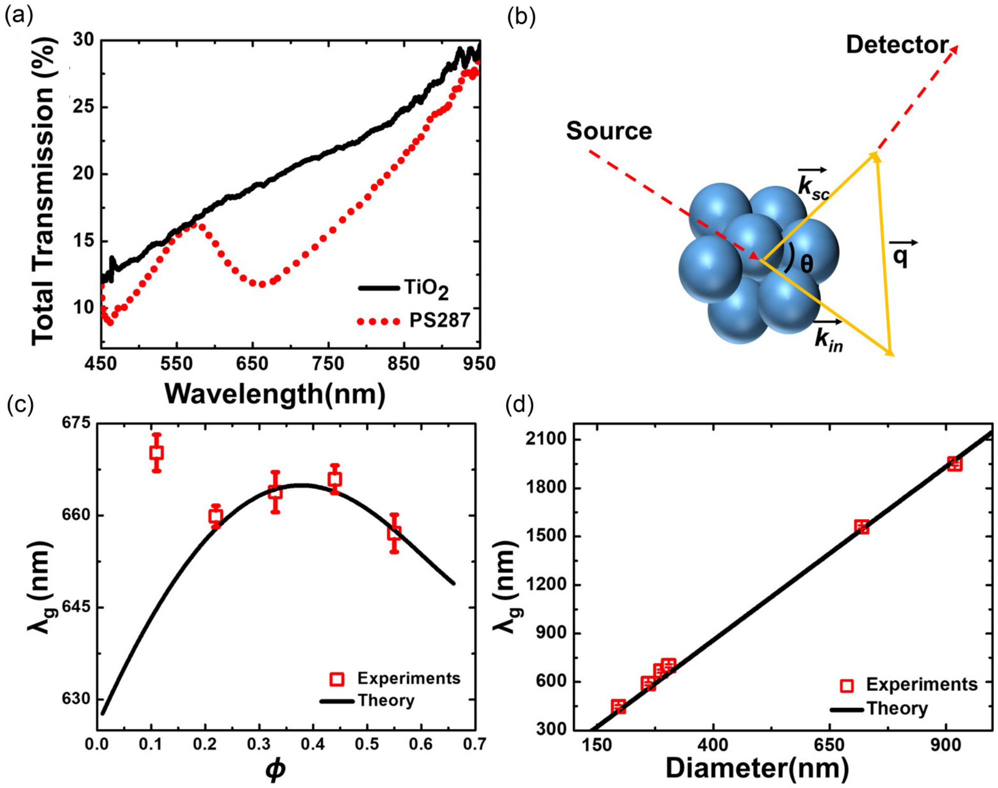

FIG. 2. (a) The measured total transmission spectra for the PS287 sample (dotted line) depict the frequency gap (λ_g) at 655 nm which is absent for the polydisperse TiO$_2$ film (solid line). (b) The schematic of the scattering model used in the calculations of λ_g. (c) The measured (open squares) and calculated (solid line) λ_g as a function of fill fraction (ϕ). (d) The measured (open squares) and calculated (solid line) λ_g as a function of scatterer diameter.

$\frac{2\pi n_{\mathrm{eff}}}{\lambda}$, where λ is the free-space wavelength (see Appendix B). The n_{eff} value is calculated using the Maxwell-Garnett theory, $n_{\mathrm{eff}} = n_{\mathrm{air}}\sqrt{\frac{2n_{\mathrm{air}}^2+n_s^2+2\phi(n_s^2-n_{\mathrm{air}}^2)}{2n_{\mathrm{air}}^2+n_s^2-\phi(n_s^2-n_{\mathrm{air}}^2)}}$, where n_{air} and n_s are the refractive indices of air and scatterers, respectively [32]. The estimation of n_{eff} using effective medium approximations is often debatable for their validity and, therefore, we have compared different available theories for the calculation of n_{eff} (see Appendix C). We found that the calculated λ_g value using the n_{eff} value obtained from the Maxwell-Garnett effective medium approximation is best fitted with the measured λ_g values in comparison to other models (see Appendix C). The sample discussed here has low index contrast and, therefore, the measured λ_g values can be compared with calculated λ_g values obtained using the n_{eff} values from the Maxwell-Garnett theory even though the sample has a high ϕ value. In fact, the Maxwell-Garnett theory has also been applied for photonic crystal and biomimetic systems which have very high ϕ values [33,34].

The resonant scattering of light is governed by the form factor [$F(q)$] and structure factor [$S(q)$] [11]. The $F(q)$ defines the individual scattering information from each scatterer within the cluster. The interference between the scattered light from each scatterer in the cluster is imputed by the $S(q)$ value [17,18]. The $S(q)$ value is calculated using the solution of the Ornstein-Zernike equation with the Percus-Yevick closure approximation (see Appendix B) [35]. The presence of a peak in the calculated $S(q)$ spectra at a particular value of $q = q_0$ is related to λ_g. It occurs when the phase difference between the scattered light from adjacent scatterers is an integer multiple of 2π. The λ_g value is calculated using the equation

$$\lambda_g = \frac{4\pi n_{\mathrm{eff}} d}{y_0} \sin\left(\frac{\theta}{2}\right), \tag{1}$$

where d is the distance between the scatterers which is equal to the mean diameter of scatterers and $y_0(= q_0 d)$ is obtained from the peak value of the calculated $S(q)$ spectra (see Appendix B). The $S(q)$ value depends on ϕ and, therefore, the value of λ_g. Figure 2(c) shows the variation of measured (open squares) and calculated (solid line) λ_g as a function of ϕ for the PS287 sample. Good agreement between the measured and calculated λ_g is seen for $\phi \geqslant 0.2$. The measured λ_g deviates from the calculated values for $\phi \leqslant 0.2$ which is due to the negligible spatial correlation between scatterers. Samples with such low ϕ values hinder the formation of strong resonant scattering which is supported by a feeble peak in the calculated $S(q)$ spectra (see Appendix B). However, the measured transmission spectra depict a shallow drop in the transmitted light at 670 nm as seen in Fig. 2(c) for $\phi \leqslant 0.2$. This highlights the fact that sufficient spatial correlation among scatterers in the sample is necessary to have a strong drop in transmission which is validated by the $S(q)$ calculations for samples with high ϕ values (see Appendix B). The transmittance value at λ_g decreases with an increase in the value

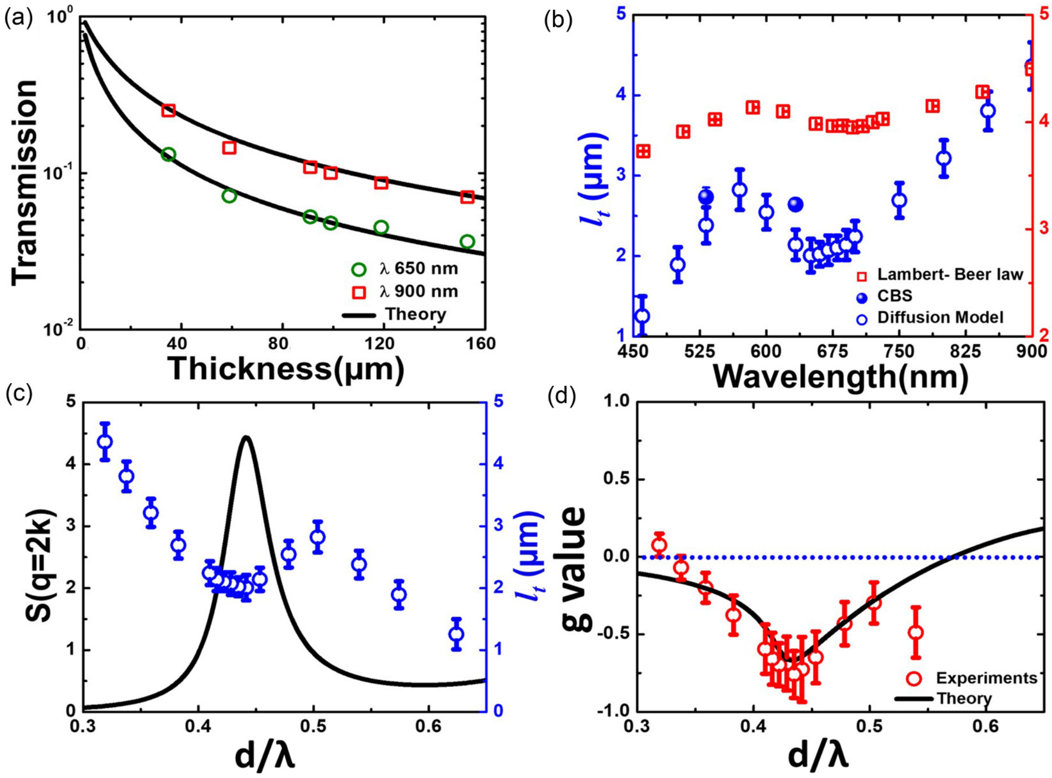

FIG. 3. (a) The measured total transmission values fitted with a solution to the diffusion approximation (solid line) to extract the l_t values at 650 nm (open circles) and 900 nm (open squares). (b) The estimated values of l_t and l_s as a function of wavelength. The l_s is obtained using the Lambert-Beer law (open squares), whereas l_t is obtained using the solution to diffusion approximation (open circles) and CBS cone (solid spheres). (c) The comparison between the l_t (symbol) and the structure factor $S(q)$ (line) values for the PS287 sample (d) The measured (symbol) and calculated (line) wavelength-dependent anisotropic scattering (g) value for the PS287 sample with a ϕ value of 0.55.

of ϕ due to the buildup of spatial correlation between the scatterers. The λ_g shows a slight redshift with an increase in ϕ value and attains a maximum λ_g value for $\phi = 0.35$ and, thereafter, it reduces for $\phi > 0.35$. The parabolic variation of λ_g is related to the variation of the ratio n_{eff}/y_0, which is precisely controlled through the ϕ value. The dependence of y_0 on ϕ is obtained from the calculated $S(q)$ values for the PS287 sample (see Appendix B). Figure 2(d) depicts the variation of measured (open squares) and calculated (solid line) λ_g as a function of d for $\phi = 0.55$. This linear scaling of λ_g is commendable, similar to the stopgap scaling in photonic crystals [4]. This is expected as both frequency gaps convey the absence of optical states within the sample at λ_g.

The frequency gap in the light transport should result in a reflection of a particular color which is precluded due to strong background multiple scattering. Therefore, the wavelength-dependent l_t and l_s values are required to further study the role of structural correlation among scatterers. The l_t value is obtained by fitting the diffusion equation to the measured L-dependent total transmission values (see Appendix D). The sample is assumed to be in a slablike geometry with x and y dimensions much larger than the z dimension ($z = 0$ to $z = L$) with a delta source at $z = z_p$ and, therefore, the 3D diffusion equation reduces to one dimension [36]:

$$\frac{\partial^2 \rho}{\partial z^2} - \frac{\rho}{L_a^2} = -\frac{1}{D} I_0 \delta(z - z_p), \tag{2}$$

where ρ is energy density in the stationary state, I_0 is the incident light intensity, D is the diffusion constant, and L_a is the absorption length. The solution to Eq. (2) in the absence of absorption ($L_a \gg L$) is approximated as the L-dependent total transmission (T_T) as [23,36]

$$T_T = \frac{l_t + z_{e1}}{L + z_{e1} + z_{e2}}, \tag{3}$$

where z_{e1} and z_{e2} are the extrapolation lengths given by $z_{e1} = \frac{2}{3} l_t (\frac{1+R}{1-R})$ and $z_{e2} = 0.7 l_t$, where R is the angle- and polarization-averaged specular reflectivity from the sample surface [37]. The R value used in the calculation is 0.40 for $\phi = 0.55$. The measured T_T value shows a decrease with an increase in the L value which signifies the photonic Ohm's law $T_T \propto l_t/L$ (see Appendix D). Figure 3(a) shows the measured T_T values at 650 nm (open circles) and 900 nm (open squares) along with the fit (solid line) using Eq. (3) as a function of the L value. Here 650 nm corresponds to λ_g whereas 900 nm corresponds to the long-wavelength limit for the PS287 sample. The estimated l_t value is 2.0 ± 0.2 μm and 4.4 ± 0.3 μm at 650 and 900 nm, respectively, which is much smaller than the L value that supports the diffusive propagation ($\lambda \ll l_t \ll L$). The l_t values are also obtained directly using the coherent backscattering (CBS) cone measurements at 532 and 633 nm which are fitted using a diffusion slab model to estimate the l_t value (see Appendix E) [18]. The l_t values obtained from the CBS cone are 2.7 ± 0.1 μm at 532 nm and 2.6 ± 0.2 μm at 633 nm, which are in close agreement with l_t values obtained using Eq. (3). The l_s value is estimated using the Lambert-Beer law: $T = T_0 e^{-L/l_s}$ where T is the ballistic transmission and T_0 is the transmission value at the interface ($z = 0$) of the sample [24]. Figure 3(b) shows a similar wavelength-dependent variation of l_s (open squares), l_t (open circles) values along with the l_t value obtained from the CBS cone (solid sphere) for the PS287 sample. The estimated l_s value is 3.9 ± 0.1 μm at 650 nm, whereas it is 4.3 ± 0.1 μm at 900 nm. It is observed that the l_t and l_s values show an appreciable drop at λ_g in comparison to wavelengths on either side of λ_g.

Figure 3(c) shows the variation of l_t and the $S(q = 2k)$ values as a function of scaled frequency (d/λ) for the PS287 sample. The $S(q)$ value is peaked at $d/\lambda = 0.45$ which exactly coincides with the trough in the l_t values, which is originated due to the frequency gap. This authorizes the role of short-range order in the sample which enhances scattering cross section σ^* and thus reduces the l_t value at λ_g. The wavelength-dependent variation of l_s and l_t values shows dissimilar values except in the long-wavelength limit ∼900 nm. The l_s value is always higher than the l_t value, which is a signature of negative g values. Therefore, to gain further insight into the anisotropic scattering, the g value is calculated as [12,17]

$$\frac{l_t}{l_s} = \frac{1}{1-g} = 2k_o^2 \frac{\int_0^{2k_o} F(q)S(q)q\,dq}{\int_0^{2k_o} F(q)S(q)q^3\,dq}. \tag{4}$$

The $F(q)$ is governed by the differential scattering cross section of a single scatterer which is given by $F(q) = k_o^2(\frac{d\sigma}{d\Omega})$ where $k_o = 2\pi/\lambda$ (see Appendix F) [11]. The scatterers are assumed to be independent of each other in the $F(q)$ calculation so that $\frac{d\sigma}{d\Omega}$ is obtained whereas $S(q)$ is associated with the interference of waves scattered from the cluster with short-range order. In experiments, the wavelength-dependent g value is estimated using the measured values of l_s and l_t. Figure 3(d) shows the measured (symbol) and calculated (solid line) wavelength-dependent g values for the PS287 sample. The measured g value is -0.7 ± 0.2 at λ_g, which is in complete agreement with the calculated g value of -0.7 for $\phi = 0.55$. The observation of the negative g value at λ_g is related to the enhanced value of σ^* due to collective resonant scattering induced by the local short-range order. On either side of λ_g, the g value increases toward the positive values which designates the dominance of isotropic scattering with $g \geqslant 0$. The negative g value is indicative of the strong backward scattering which indicates the proximity toward the Anderson localization with $\lambda \sim l_t$ [17,38]. Though we have observed the negative g values in our samples, but we are not in the regime of light localization. However, we have discussed the mechanism that leads to negative g values through engineering the l_t and l_s values using samples with short-range order. The value of g is ϕ dependent through its dependence on the $S(q)$ value (see Appendix F). This suggests that the proper tuning of ϕ can control the l_t and l_s values, and hence the negative g value.

We would also like to emphasize that the present results are applicable in general for any kind of wave transport such as the acoustic or matter wave at the relevant length scales. Further, the observation of negative g value indicates an inclination to Anderson localization [38], and the results put forward an alternative direction of localization in samples with coexistence of order and disorder [39]. Recently, many natural biogenic species have exhibited short-range order and the present results are useful in analyzing their scattering properties with the possibility to observe negative g values. The frequency gap could also exhibit reduced photon density of states and this will be useful for quantum electrodynamics experiments such as controlled emission using single emitters. The results are also applicable in the broad area of condensed matter physics such as the disorder-induced process in superconductivity, magnetic materials, Bose-Einstein condensate, and liquid metal [40–43]. Therefore, our results apply for a range of areas spanning from condensed matter physics, including soft materials and the optical domain, to aid in understanding new physical processes induced by the spatially correlated scatterers with short-range order in the relevant wavelength scales.

III. CONCLUSIONS

In summary, we have studied a tunable frequency gap associated with three-dimensional photonic structures with short-range order made using monodisperse scatterers. The scattering model based on the structural morphology of the sample reveals the frequency gap that is originated due to the interference of collective scattering events induced by local short-range order. This is further confirmed using the structure factor calculations wherein the structure factor peak is coinciding with the measured frequency gap that supports the role of local short-range order. We have obtained negative anisotropy scattering values at the frequency gap which is supported by theoretical calculations. Therefore, the photonic structures with short-range order provide a feasible route to achieve the rarely observed negative anisotropy scattering values in the visible wavelength region. The presented results are not limited to photonic systems; rather it has general applicability in other kinds of wave transport such as the acoustic and matter waves, and many areas of disorder-induced processes in condensed matter systems.

ACKNOWLEDGMENTS

The financial support from IIT Ropar (ISIRD Grant No. 2014), DST-SERB (Grant No. FTS/PS-80/2014), and CSIR [Grant No. 03(1352)/16/EMR-II], Government of India, is gratefully acknowledged. S.K.S. thanks MeitY, Government of India, for support through the Visvesvaraya Ph.D. fellowship. The authors also would like to acknowledge IIT Ropar for the use of central research facilities. We also thank Dr. Priya and Sachin Sharma for fruitful discussions.

APPENDIX A: SAMPLE SYNTHESIS AND EXPERIMENTAL DETAILS

The samples are synthesized using the colloidal suspension consisting of 2.5 wt % monodisperse polystyrene (PS) beads (MicroParticles GmbH) of submicron diameter. The beads are negatively charged and, therefore, the repulsive Coulombic forces between beads ensure that the beads do not collide with each other in the suspension and are stable

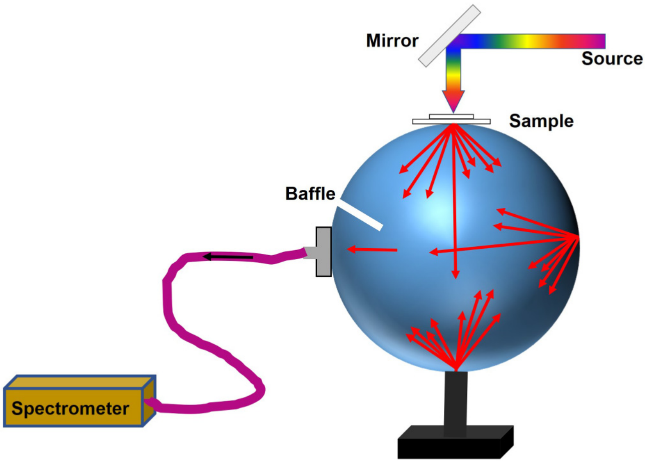

FIG. 4. The schematic view of the total transmission measurement setup using a white light source along with an integrating sphere. The collected light is sent through a fiber to the minispectrometer.

in the suspension. The repulsive Coulombic force between the micron-sized beads can be weakened by adding a positive electrolyte such as calcium chloride ($CaCl_2$) so that the self-assembling of PS beads can be precisely manipulated. The addition of 0.1 M $CaCl_2$ to the PS suspension gives rise to a net attractive force between the microbeads. This results in the formation of clusters induced by the flocculation of beads in the suspension [44]. The colloidal suspension is quite stable and the sample synthesis is repeatable and reproducible. The fill fraction (ϕ) of the sample is controlled with volume fractions of the scatterers during the sample synthesis process. Samples are synthesized using different bead diameters (d) and different ϕ values which result in samples with different values of effective refractive index (n_{eff}).

The structural morphology of the samples is studied using a scanning electron microscope (JEOL JSM-6610 LV). The thickness (L) of the samples is measured using a profilometer (Bruker DektakXT) with the substrate as the reference point. Figure 4 shows a schematic view of the home-built setup used to measure the total transmission of light through the samples. A broadband light from the supercontinuum (Fianium White-Lase Micro) is incident on the sample which is kept at the entrance port of the integrating sphere (Labsphere). The light transmitted through the samples is collected using an integrating sphere which is connected to a fiber-coupled spectrometer (Avantes). The CBS cone measurements are performed using 532- and 633-nm diodes and a He-Ne laser, respectively The circularly polarized light made using a quarter-wave plate is incident on the sample and the scattered light is collected using a charge-coupled device (CCD) camera (DCU224C Thorlabs).

APPENDIX B: STRUCTURE FACTOR [$S(q)$] AND FREQUENCY-GAP WAVELENGTH (λ_g) CALCULATIONS

The structure factor [$S(q)$] provides statistical information about the scatterers arrangement in q space which is given by

$$S(q) = \frac{1}{n}\sum_{i,j} e^{-i\vec{q}(\vec{y}_j-\vec{y}_i)}, \tag{B1}$$

where n is the number density of scatterers; y_i and y_j are the spatial positions of the scatterers. The $S(q)$ value is calculated using the solution of the Ornstein-Zernike equation with the Percus-Yevick closure approximation for a hard sphere (in our case PS beads) [35,45]. We have used the following analytical expression for the $S(q)$ calculation:

$$S(q) = \frac{1}{1-c(q,\phi)}, \tag{B2}$$

with

$$\begin{aligned} c(q,\phi) = {} & -24\phi\frac{(1+2\phi)^2}{(1-\phi)^4}\frac{\sin q - q\cos q}{q^3} - 6\phi\frac{-\left(1+\frac{\phi}{2}\right)^2}{(1-\phi)^4}\frac{q^2\cos q - 2q\sin q - 2\cos q + 2}{q^4} \\ & - \phi\frac{(1+2\phi)^2}{(1-\phi)^4}\frac{q^4\cos q - 4q^3\sin q - 12q^2\cos q + 24q\sin q + 24\cos q - 24}{q^6}. \end{aligned}$$

Figure 5(a) shows the $S(q)$ plot for the PS287 sample with $\phi = 0.55$ as a function of q, which is obtained using Eq. (B2). The first peak of the $S(q)$ spectra at q_o corresponds to the average spacing between the coordination shells $a = \frac{2\pi}{|q|}$ which is schematically shown in the inset of Fig. 5(a).

Figure 5(b) shows the $S(q)$ for the PS287 sample as a function of the dimensionless variable $y = qd$ for different values of ϕ (0.11–0.55). It is seen that with an increase in the ϕ value, the intensity of the interference peak at $y_0 = q_0 d$ increases along with a redshift in the peak position, which is primarily responsible for the observed shift in the frequency gap. The transmission spectra show a shallow dip for samples with $\phi = 0.11$ due to the weak spatial correlation between the scatterers. With an increase in the ϕ value, the transmission dip becomes stronger due to the strong spatial correlation between the scatterers. Figure 5(c) depicts the d-dependent $S(q)$ plot for the samples with a fixed value of $\phi = 0.55$. The $S(q)$ peaks are having the same intensity whereas the position of the y_0 peak is redshifted with an increase in the d value, which further validates the frequency gap scaling with d. The frequency gap (λ_g) wavelength can be calculated using the peak position value from the $S(q)$ calculation. Consider the scattering geometry as shown in Fig. 2(b); we have

$$\begin{aligned} \vec{k}_{\text{sc}} &= \vec{q} + \vec{k}_{\text{in}}, \\ |\vec{q}|^2 &= |\vec{k}_{\text{in}}|^2 + |\vec{k}_{\text{sc}}|^2 - 2\vec{k}_{\text{sc}}\cdot\vec{k}_{\text{in}}. \end{aligned}$$

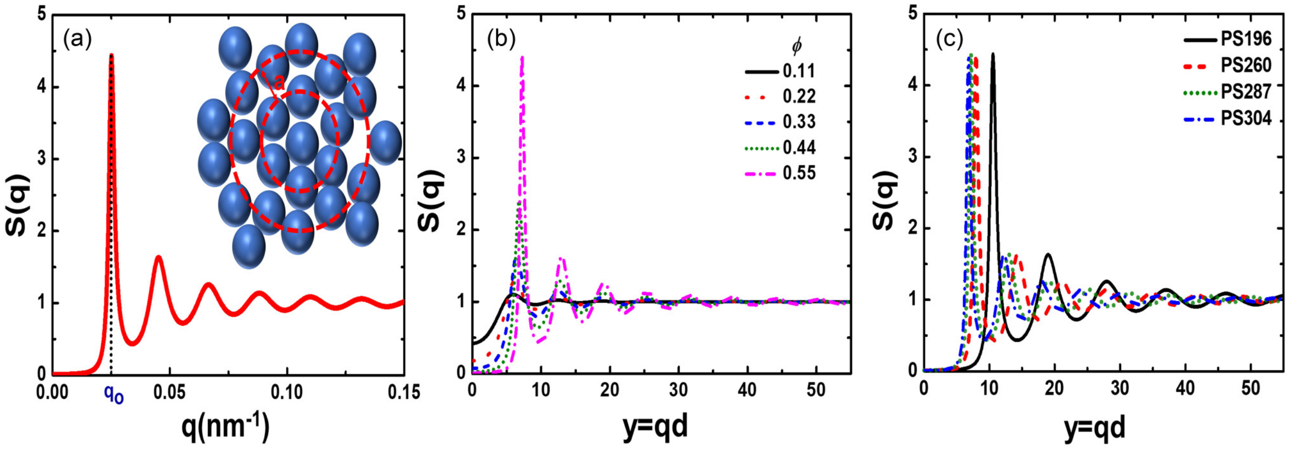

FIG. 5. (a) The calculated $S(q)$ spectra for the PS287 sample with $\phi = 0.55$. Inset: Schematic of the spatial arrangement of the scatterers, where the average spacing between coordination shells (dashed line) is a. The calculated $S(q)$ spectra (b) for different ϕ values for fixed d value and (c) for different d values for the scatterers with fixed ϕ value.

We assume elastic scattering, so that $\vec{k}_{\text{in}} = \vec{k}_{\text{sc}} = \vec{k} = |k|$; hence

$$q^2 = 2k^2[1-\cos(\theta)], \quad q^2 = 4k^2\sin^2\left(\frac{\theta}{2}\right),$$

$$q = 2k\sin\left(\frac{\theta}{2}\right), \tag{B3}$$

$$\lambda_g = \frac{4\pi n_{\text{eff}} d}{y_0}\sin\left(\frac{\theta}{2}\right). \tag{B4}$$

The value of y_0 is obtained from the peak position of the $S(q)$ spectra.

APPENDIX C: ESTIMATION OF n_{eff} VALUE

Various effective medium approximations have been proposed for the estimation of the effective refractive index (n_{eff}) or the effective dielectric constant (ε_{eff}) value [46]. Here we compare three important models such as the scalar, Maxwell-Garnett (MG), and the coherent potential approximation (CPA) for the n_{eff} calculation [47,48]. All these models assume that the scatterers with a dielectric constant ε_2 are embedded in a background dielectric medium of dielectric constant ε_1. The scalar model is the simplest method for the estimation of the ε_{eff} value which is defined as $\varepsilon_{\text{eff}} = \varepsilon_1(1-\phi) + \varepsilon_2\phi$. However, the scalar method is more adequate for samples with high values of ϕ such as the self-assembled photonic crystals ($\phi = 0.74$). Another widely used approach is the MG model. The ε_{eff} is calculated according to the MG model as $\varepsilon_{\text{eff}} = \varepsilon_1(\frac{2\varepsilon_1+\varepsilon_2+2\phi(\varepsilon_2-\varepsilon_1)}{2\varepsilon_1+\varepsilon_2-\phi(\varepsilon_2-\varepsilon_1)})$. The MG model gives a more realistic picture than the scalar method because it considers the cumulative polarizabilities of the scatterers, and not their refractive indices [47]. The CPA theory is an alternative approach used to estimate the ε_{eff} value which is defined as $\frac{3(1-\phi)}{2+\frac{\varepsilon_1}{\varepsilon_{\text{eff}}}} + \frac{3\phi}{2+\frac{\varepsilon_2}{\varepsilon_{\text{eff}}}} = 1$ [48].

Figure 6(a) shows the variation of n_{eff} values as a function of ϕ calculated using different models similar to those considered by Soukoulis *et al.* [48]. The n_{eff} values obtained using the scalar approximation method (solid line) are always higher than those obtained from the other methods and increase linearly with an increase in ϕ values. The MG approximation is not a symmetric method and therefore two cases are

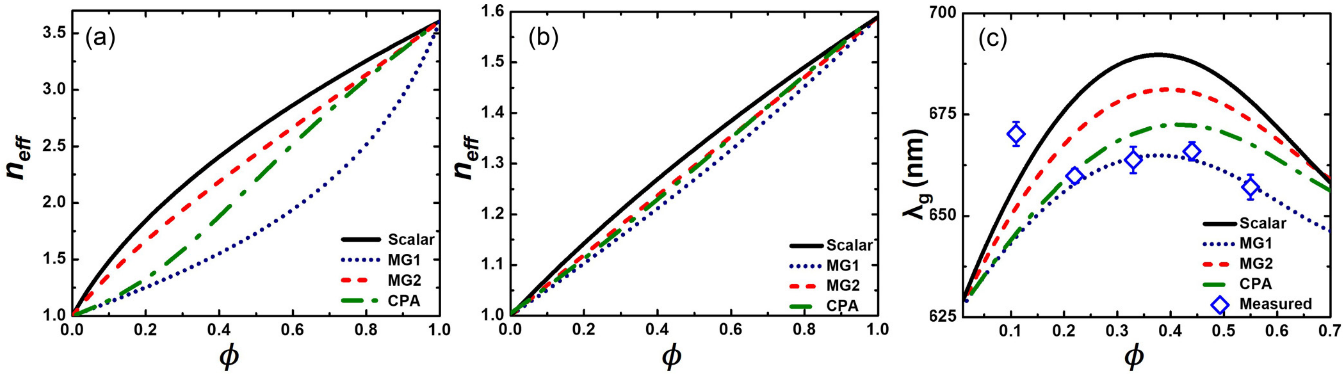

FIG. 6. (a) The estimated n_{eff} as a function of the ϕ values for samples made with scatterers of refractive index of (a) 3.60 and (b) 1.6. The n_{eff} values are obtained using three effective medium approximations such as scalar (solid line), MG1 (short dotted line), MG2 (short dashed line), and CPA (dash-dotted line). (c) A comparison between the measured (symbols) and calculated (lines) λ_g as a function of ϕ for all the considered effective medium approximations.

considered here. In Fig. 6(a), the MG1 model (dotted line) represents the case where $\varepsilon_1 = 1$, $\varepsilon_2 = 13$ and ϕ is the volume fraction of the ε_2 material whereas in the MG2 model (dashed line), we take $\varepsilon_1 = 13$, $\varepsilon_2 = 1$ and now ϕ is the volume fraction of the ε_1 material. The n_{eff} values for both the MG1 and MG2 models increases with an increase in the ϕ value, but for a particular value of ϕ both cases have a noticeable difference. The n_{eff} value estimated using the CPA method (dash-dotted line) also increases with an increase in the ϕ values with n_{eff} values appearing between the MG1 and MG2 curves. It is noticed that for $\phi < 0.2$, the n_{eff} values are very close to the values obtained using the MG1 method and for high values of $\phi > 0.7$, the n_{eff} values coincideg with those obtained using the MG2 method.

Figure 6(b) shows the estimated n_{eff} values as a function of ϕ for the sample considered in the present work made using PS scatterers of refractive index 1.6. Similar to Fig. 6(a), the n_{eff} values obtained using the scalar method are always higher in comparison to other models for any values of ϕ. The MG1 and MG2 models show similar variation in the n_{eff} values. However, due to the low index contrast of the sample, the difference between the n_{eff} values for both cases is very minimal. The n_{eff} values obtained from the CPA method are partly overlapping with the n_{eff} values estimated from the MG1 and MG2 approach. We can conclude that for samples with less index contrast, all the models give similar variation of n_{eff} with the ϕ value.

Figure 6(c) shows the calculated (lines) variation of λ_g obtained using the n_{eff} values from the different effective medium approximation along with the measured λ_g values (symbols) as a function of ϕ value. The measured λ_g values are in good agreement with the calculated λ_g values obtained using the n_{eff} values from the MG1 method. Therefore, we use the n_{eff} value from the MG1 method for the analysis. However, for very low values of $\phi = 0.11$, the measured λ_g values are not in agreement with the calculated λ_g values obtained using any of the n_{eff} values from different methods. At such low ϕ values, the scatterers are not spatially correlated, which results in very weak resonant scattering which is also evidenced by the calculated $S(q)$ spectra with a negligible peak and much less intensity as seen in Fig. 5(b) (solid line). In fact, in the experiments also, we have observed a shallow dip at 670 nm with a little decrease in the transmitted light. This data point is shown in Fig. 2(c) to highlight the fact that when the spatial correlation between the scatterers is negligible, a shallow drop in the transmitted light intensity is observed and it will be difficult to fit the measurements to the calculated λ_g values in samples with the low amount of scatterers.

APPENDIX D: DIFFUSION APPROXIMATION

The diffuse light propagates in the sample according to the diffusion equation given by [49]

$$\nabla^2 I(r) - \alpha^2 I(r) = -\frac{1}{D} S(r), \tag{D1}$$

where D is the diffusion constant, $\alpha(= 1/L_a)$ is the inverse absorption length, and $S(r)$ is the source. To obtain the stationary solution for Eq. (D1), we have considered a disordered medium with a certain thickness (L) in the slab geometry, as shown in Fig. 7(a). The boundary conditions are required

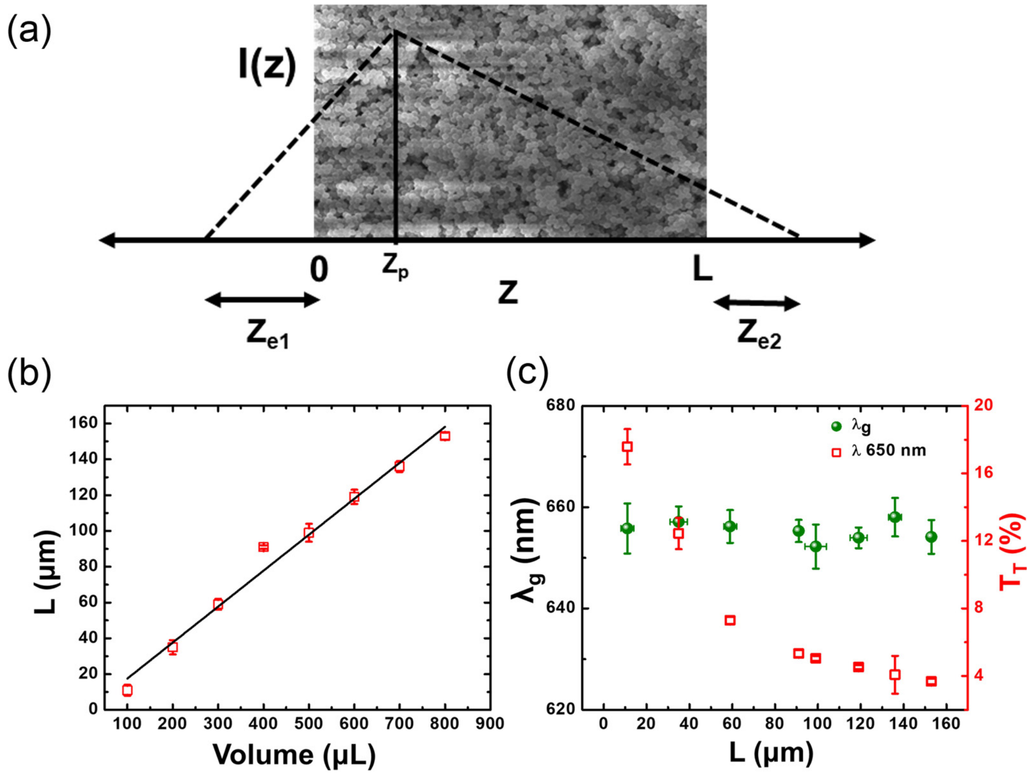

FIG. 7. (a) Schematic of the slab geometry considered to solve the diffusion approximation. The dashed line represents the solution of the diffusion equation. (b) The variation of L value with an increase in the volume of the scatterers in the sample. (c) The variation of λ_g (left axis) and T_T value (right axis) with an increase in the L value of the sample.

for diffusion approximation which gives rise to extrapolation lengths z_{e1} and z_{e2} as shown in Fig. 7(a). The boundary conditions for the system are

$$I(z) = 0\begin{cases} z = -z_{e1} \\ z = z_{e2} + L \end{cases}. \tag{D2}$$

The value of $z_{e1,2}$ may be different at the front and back surfaces of the sample depending on the surface reflectivity. The stationary diffusion equation can be solved using a delta source at $z = z_p$ (the penetration depth) with the following boundary conditions [49]:

$$I(z) = I(z_p)\begin{cases} \frac{\sinh[(\alpha(z_{e1}+z))]}{\sinh[(\alpha(z_p+z_{e1}))]} z < z_p \\ \frac{\sinh[(\alpha(L+z_{e2}-z))]}{\sinh[(\alpha(L+z_p+z_{e2}))]} z > z_p \end{cases}, \tag{D3}$$

where

$$I(z_p) = \frac{S(0)}{\alpha D}\frac{\sinh[\alpha(z_p + z_{e1})]\sinh[\alpha(L + z_{e2} - z_p)]}{\sinh[\alpha(L + z_{e1} + z_{e2})]}. \tag{D4}$$

$z_{ei} = \frac{1}{2\alpha}\ln(\frac{1+\alpha z_{oi}}{1-\alpha z_{oi}})$, where $i = 1$ and 2 represent the front and back surface of the sample, respectively, and $z_{oi} = \frac{2}{3}l_t(\lambda)(\frac{1+R_i}{1-R_i})$. Here R_i are the polarization-dependent angle-averaged reflectivity values at the boundaries of the sample.

The T_T is the total light intensity integrated over all angles, which is the ratio of total light collected at $z = L$ to the incident light [49]:

$$T_T = \frac{1 - R}{\alpha}\frac{\sinh[\alpha(z_p + z_{e1})]\sinh[\alpha(z_{e2})]}{\sinh[\alpha(L + z_{e1} + z_{e2})]}. \tag{D5}$$

If $L \gg l_t$ and $L_a \gg L$, then Eq. (D5) can be approximated as

$$T_T = \frac{l_t + z_{e1}}{L + z_{e1} + z_{e2}}\alpha\frac{l_t}{L}, \tag{D6}$$

where $z_e \sim l_t$. Equation (D6) signifies that T_T is directly proportional to the l_t value and inversely proportional to the L value. Figure 7(b) depicts the measured L value of the sample as a function of the volume fractions of PS beads with a concentration of 2.5 wt%. The measured L value is 11± 2 μm for a minimum volume (100 µl) of the solution and for maximum volume (800 µl) of the solution, the measured L value is 152 ± 3 μm. Figure 7(c) shows the variation of λ_g obtained from the T_T spectra as a function of the L value. The λ_g (closed symbols) is found to be independent of L value and fluctuates in the range of $650 < \lambda_g < 665$ nm, which confirms the uniform growth of the samples. The T_T (open symbols) value at λ_g is 17 ± 1% for the sample with $L = 11 \pm 3\,\mu$m which is reduced to 3.0 ± 0.5% for the sample with $L = 152 \pm 2\,\mu$m. It can be observed that the T_T value at λ_g decreases exponentially with an increase in the sample L value. The fit of Eq. (D6) to the L-dependent T_T values at specific wavelengths is shown in the Fig. 3(a).

APPENDIX E: MODEL FOR THE COHERENT BACKSCATTERING CONE

The CBS cone provides the scattering length scale (l_t) of the medium. The full width at half maxima of the CBS cone at a certain wavelength is given by $\sim 0.7/kl_t$ [50]. To evaluate the l_t, the measured CBS cone is fitted using a function given by Eq. (E1) [50]:

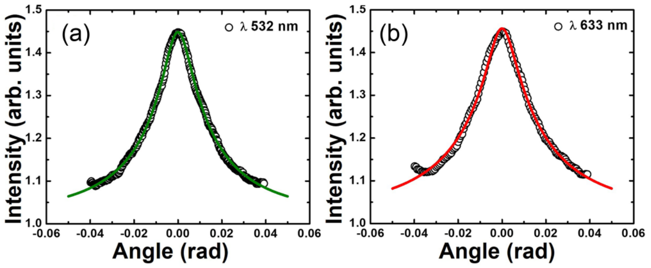

FIG. 8. The measured CBS cone (symbol) for the PS287 sample at (a) 532 nm and (b) 633 nm. To estimate the l_t values, the measured cones are fitted (solid line) using Eq. (E1).

$$I(\theta) = 1 + (A - 1)\frac{\gamma_c(\theta)}{\gamma_l}, \tag{E1}$$

where A is the experimental enhancement factor, and its value deviates from the theoretically expected value of 2 due to the residual components of single scattering or the stray light. The γ_c is the coherent contribution of intensity that is mainly dominating in the formation of the backscattering cone and γ_l is the incoherent diffuse background intensity. The detailed expression of the γ_c for a slablike sample with a certain L value and γ_l can be found elsewhere [50]. Figures 8(a) and 8(b) show the measured CBS cone (circles) along with the fitted (solid line) curve using Eq. (E1). The estimated l_t values from the fit to the CBS cone are 2.73 ± 0.12 µm and 2.64 ± 0.18 µm at 532 and 633 nm, respectively.

APPENDIX F: ϕ-DEPENDENT ANISOTROPIC SCATTERING VALUE (g) CALCULATION

The g value calculation involves the estimation of $S(q)$ (Appendix B) and the $F(q)$ values as seen in Eq. (4). The form factor $F(q)$ for a single scatterer can be calculated as [11]

$$F(q) = k_o^2\left(\frac{d\sigma}{d\Omega}\right). \tag{F1}$$

The differential scattering cross section ($\frac{d\sigma}{d\Omega}$) is the ratio of the intensity of radiant energy scattered in a given direction to that for the incident light per unit area per unit solid angle. The ($\frac{d\sigma}{d\Omega}$) for incident light is given by [11]

$$\frac{d\sigma}{d\Omega} = \frac{\pi}{k_o^2}[|S_1(\theta_s)|^2 + |S_2(\theta_s)|^2], \tag{F2}$$

where

$$S_1(\theta_s) = \sum_{n=1}^{\infty}\frac{2n+1}{n(n+1)}[a_n\pi_n(\cos\theta_s) + b_n\tau_n(\cos\theta_s)],$$

$$S_2(\theta_s) = \sum_{n=1}^{\infty}\frac{2n+1}{n(n+1)}[a_n\tau_n(\cos\theta_s) + b_n\pi_n(\cos\theta_s)].$$

S_1 and S_2 are the scattered field amplitudes and θ_s is the polar scattering angle with respect to the incident light. The a_n and b_n are the Mie coefficients of the single scatterer to calculate the amplitudes of the scattered field. The coefficients of a_n and b_n are defined as [11]

$$a_n = \frac{m^2 j_n(mx)[x j_n(x)]' - j_n(x)[mx j_n(mx)]'}{m^2 j_n(mx)[x h_n(x)]' - h_n(x)[mx j_n(mx)]'},$$

$$b_n = \frac{j_n(mx)[x j_n(x)]' - j_n(x)[mx j_n(mx)]'}{j_n(mx)[x h_n(x)]' - h_n(x)[mx j_n(mx)]'},$$

where m is the refractive index, $x = ka$ is the corresponding size parameter, and a ($d/2$) is the scatterer radius. The $j_n(z)$ and $h_n(z)$ are spherical Bessel and Hankel functions of the first kind of order n with respect to the argument z, respectively. The functions π_n and τ_n describe the angular scattering patterns of the spherical harmonics which are defined as [11]

$$\tau_n(\cos\theta) = -\frac{dp_n^1(\cos\theta)}{d\theta}, \quad \pi_n(\cos\theta) = -\frac{p_n^1(\cos\theta)}{\sin\theta}.$$

Figure 9 shows the calculated anisotropy scattering value (g) as a function of scaled frequency for $0.15 \leqslant \phi \leqslant 0.65$. It is observed that the ϕ value of the sample strongly influences the g values. The g values are found to be positive for $\phi \geqslant 0.15$, because a smaller number of scatterers are not able to establish structural correlation among themselves, which leads to an isotropic scattering. As the density of scatterers increases with an increase in the ϕ value, the short-range order in the sample is developed due to the positional correlation among the scatterers. Therefore, a dip in the calculated g value at the scaled frequency of 0.45 arises, which corresponds to the frequency gap of the sample. The negative g value is indicating the backward scattering from the sample at the frequency gap, and it is increasing with an increase in ϕ values. Hence, it is possible to tune the scattering length scales of the sample with a controlled density of scatterers.

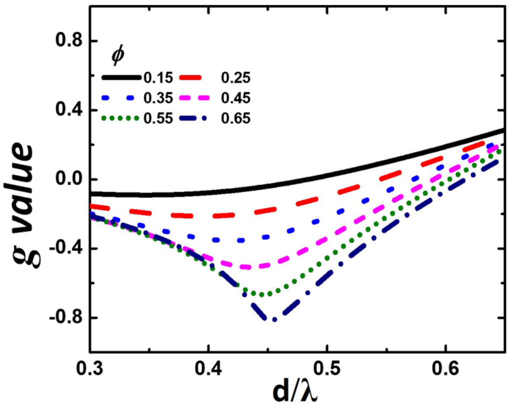

FIG. 9. The ϕ-dependent g values as a function of wavelength for the PS287 sample.

---

[1] K.-H. Lin, C.-M. Lai, C.-C. Pan, J.-I. Chyi, J.-W. Shi, S.-Z. Sun, C.-F. Chang, and C.-K. Sun, Spatial manipulation of nanoacoustic waves with nanoscale spot sizes, Nat. Nanotechnol. **2**, 704 (2007).

[2] G. Chen, *Nanoscale Energy Transport and Conversion: A Parallel Treatment of Electrons, Molecules, Phonons, and Photons* (Oxford University Press, Oxford, 2005).

[3] C.-Z. Ning, L. Dou, and P. Yang, Bandgap engineering in semiconductor alloy nanomaterials with widely tunable compositions, Nat. Rev. Mater. **2**, 1 (2017).

[4] J. D. Joannopoulos, S. G. Johnson, J. N. Winn, and R. D. Meade, *Molding the Flow of Light* (Princeton University Press, Princeton, NJ, 2008).

[5] P. W. Anderson, Absence of diffusion in certain random lattices, Phys. Rev. **109**, 1492 (1958).

[6] R. Brown, Resonance scattering and the electrical and thermal resistivities associated with extended defects in crystals, Phys. Rev. **156**, 692 (1967).

[7] D. S. Wiersma, Disordered photonics, Nat. Photonics **7**, 188 (2013).

[8] H. Yılmaz, C. W. Hsu, A. Yamilov, and H. Cao, Transverse localization of transmission eigenchannels, Nat. Photonics **13**, 352 (2019).

[9] L. Schertel, L. Siedentop, J. M. Meijer, P. Keim, C. M. Aegerter, G. J. Aubry, and G. Maret, The structural colors of photonic glasses, Adv. Opt. Mater **7**, 1900442 (2019).

[10] A. Ishimaru, *Wave Propagation and Scattering in Random Media* (Academic Press, New York, 1978), Vol. 2.

[11] C. F. Bohren and D. R. Huffman, *Absorption and Scattering of Light by Small Particles* (John Wiley & Sons, New York, 2008).

[12] S. Fraden and G. Maret, Multiple Light Scattering from Concentrated, Interacting Suspensions, Phys. Rev. Lett. **65**, 512 (1990).

[13] E. Akkermans, P. Wolf, R. Maynard, and G. Maret, Theoretical study of the coherent backscattering of light by disordered media, J. Phys. I **49**, 77 (1988).

[14] N. W. Ashcroft and J. Lekner, Structure and resistivity of liquid metals, Phys. Rev. **145**, 83 (1966).

[15] R. W. Hart and R. A. Farrell, Light scattering in the cornea, J. Opt. Soc. Am. **59**, 766 (1969).

[16] P. Saulnier, M. Zinkin, and G. Watson, Scatterer correlation effects on photon transport in dense random media, Phys. Rev. B **42**, 2621 (1990).

[17] L. F. Rojas-Ochoa, J. Mendez-Alcaraz, J. Sáenz, P. Schurtenberger, and F. Scheffold, Photonic Properties of Strongly Correlated Colloidal Liquids, Phys. Rev. Lett. **93**, 073903 (2004).

[18] X. Peng and A. Dinsmore, Light Propagation in Strongly Scattering, Random Colloidal Films: The Role of the Packing Geometry, Phys. Rev. Lett. **99**, 143902 (2007).

[19] L. Pattelli, A. Egel, U. Lemmer, and D. S. Wiersma, Role of packing density and spatial correlations in strongly scattering 3D systems, Optica **5**, 1037 (2018).

[20] G. M. Conley, M. Burresi, F. Pratesi, K. Vynck, and D. S. Wiersma, Light Transport and Localization in Two-Dimensional Correlated Disorder, Phys. Rev. Lett. **112**, 143901 (2014).

[21] R. R. Naraghi, S. Sukhov, J. Sáenz, and A. Dogariu, Near-Field Effects in Mesoscopic Light Transport, Phys. Rev. Lett. **115**, 203903 (2015).

[22] G. J. Aubry, L. Schertel, M. Chen, H. Weyer, C. M. Aegerter, S. Polarz, H. Cölfen, and G. Maret, Resonant transport and near-field effects in photonic glasses, Phys. Rev. A **96**, 043871 (2017).

[23] P. Garcia, R. Sapienza, J. Bertolotti, M. Martín, A. Blanco, A. Altube, L. Vina, D. Wiersma, and C. López, Resonant light transport through Mie modes in photonic glasses, Phys. Rev. A **78**, 023823 (2008).

[24] Priya, O. Schöps, U. Woggon, and R. V. Nair, Inhibited spontaneous emission using gaplike resonance in disordered photonic structures, Phys. Rev. A **98**, 043835 (2018).

[25] M. Xiao, Z. Hu, Z. Wang, Y. Li, A. D. Tormo, N. Le Thomas, B. Wang, N. C. Gianneschi, M. D. Shawkey, and A. Dhinojwala, Bioinspired bright noniridescent photonic melanin supraballs, Sci. Adv. **3**, e1701151 (2017).

[26] H. Noh, J.-K. Yang, S. F. Liew, M. J. Rooks, G. S. Solomon, and H. Cao, Control of Lasing in Biomimetic Structures with Short-Range Order, Phys. Rev. Lett. **106**, 183901 (2011).

[27] L. S. Froufe-Pérez, M. Engel, J. J. Sáenz, and F. Scheffold, Band gap formation and Anderson localization in disordered photonic materials with structural correlations, Proc. Natl. Acad. Sci. USA **114**, 9570 (2017).

[28] H. Yin, B. Dong, X. Liu, T. Zhan, L. Shi, J. Zi, and E. Yablonovitch, Amorphous diamond-structured photonic crystal in the feather barbs of the scarlet macaw, Proc. Natl. Acad. Sci. USA **109**, 10798 (2012); M. Rechtsman, A. Szameit, F. Dreisow, M. Heinrich, R. Keil, S. Nolte, and M. Segev, Amorphous Photonic Lattices: Band Gaps, Effective Mass, and Suppressed Transport, Phys. Rev. Lett. **106**, 193904 (2011).

[29] L. S. Froufe-Pérez, M. Engel, P. F. Damasceno, N. Muller, J. Haberko, S. C. Glotzer, and F. Scheffold, Role of Short-Range Order and Hyperuniformity in the Formation of Band Gaps in Disordered Photonic Materials, Phys. Rev. Lett. **117**, 053902 (2016).

[30] J. Ricouvier, P. Tabeling, and P. Yazhgur, Foam as a self-assembling amorphous photonic band gap material, Proc. Natl. Acad. Sci. USA **116**, 9202 (2019).

[31] V. Hwang, A. B. Stephenson, S. Magkiriadou, J.-G. Park, and V. N. Manoharan, Effects of multiple scattering on angle-independent structural color in disordered colloidal materials, Phys. Rev. E **101**, 012614 (2020).

[32] J. C. M. Garnett, Colours in metal glasses and in metallic films, Trans. Roy. Soc. **53**, 385 (1904).

[33] W. L. Vos, R. Sprik, A. van Blaaderen, A. Imhof, A. Lagendijk, and G. H. Wegdam, Strong effects of photonic band structures on the diffraction of colloidal crystals, Phys. Rev. B **53**, 16231 (1996).

[34] J. D. Forster, H. Noh, S. F. Liew, V. Saranathan, C. F. Schreck, L. Yang, J. G. Park, R. O. Prum, S. G. Mochrie, and C. S. O'Hern, Biomimetic isotropic nanostructures for structural coloration, Adv. Mater **22**, 2939 (2010).

[35] N. Ashcroft and D. C. Langreth, Structure of binary liquid mixtures. I, Phys. Rev. **156**, 685 (1967).

[36] J. G. Rivas, R. Sprik, C. Soukoulis, K. Busch, and A. Lagendijk, Optical transmission through strong scattering and highly polydisperse media, EPL **48**, 22 (1999).

[37] J. Zhu, D. Pine, and D. Weitz, Internal reflection of diffusive light in random media, Phys. Rev. A **44**, 3948 (1991).

[38] B. Wang and C. Zhao, Achieving a strongly negative scattering asymmetry factor in random media composed of dual-dipolar particles, Phys. Rev. A **97**, 023836 (2018).

[39] S. John, Strong Localization of Photons in Certain Disordered Dielectric Superlattices, Phys. Rev. Lett. **58**, 2486 (1987).

[40] B. Sacépé, J. Seidemann, F. Gay, K. Davenport, A. Rogachev, M. Ovadia, K. Michaeli, and M. V. Feigel'man, Low-temperature anomaly in disordered superconductors near B_{c2} as a vortex-glass property, Nat. Phys. **15**, 48 (2019).

[41] D. Wesenberg, T. Liu, D. Balzar, M. Wu, and B. L. Zink, Long-distance spin transport in a disordered magnetic insulator, Nat. Phys. **13**, 987 (2017).

[42] A. Orlova, H. Mayaffre, S. Krämer, M. Dupont, S. Capponi, N. Laflorencie, A. Paduan-Filho, and M. Horvatić, Detection of a Disorder-Induced Bose-Einstein Condensate in a Quantum Spin Material at High Magnetic Fields, Phys. Rev. Lett. **121**, 177202 (2018).

[43] J. C. Szabo, K. Lee, V. Madhavan, and N. Trivedi, Local Spectroscopies Reveal Percolative Metal in Disordered Mott Insulators, Phys. Rev. Lett. **124**, 137402 (2020).

[44] P. D. García, R. Sapienza, and C. López, Photonic glasses: A step beyond white paint, Adv. Mater **22**, 12 (2010).

[45] N. Ashcroft and D. C. Langreth, Structure of binary liquid mixtures. II. Resistivity of alloys and the ion-ion interaction, Phys. Rev. **159**, 500 (1967).

[46] K. Dolgaleva and R. W. Boyd, Local-field effects in nanostructured photonic materials, Adv. Opt. Photonics **4**, 1 (2012).

[47] V. A. Markel, Introduction to the Maxwell Garnett approximation: Tutorial, J. Opt. Soc. Am. A **33**, 1244 (2016).

[48] C. Soukoulis, S. Datta, and E. Economou, Propagation of classical waves in random media, Phys. Rev. B **49**, 3800 (1994).

[49] N. Garcia, A. Genack, and A. Lisyansky, Measurement of the transport mean free path of diffusing photons, Phys. Rev. B **46**, 14475 (1992).

[50] M. B. Van Der Mark, M. P. van Albada, and A. Lagendijk, Light scattering in strongly scattering media: mulTiple scattering and weak localization, Phys. Rev. B **37**, 3575 (1988).